Nanotechnology **18** (2007) 175707 (8pp) doi:10.1088/0957-4484/18/17/175707

Single-step growth and low resistance interconnecting of gold nanowires

Birol Ozturk[1], **Bret N Flanders**[1,4], **Daniel R Grischkowsky**[2] **and Tetsuya D Mishima**[3]

[1] Department of Physics, Oklahoma State University, Stillwater, OK 74078, USA
[2] School of Electrical and Computer Engineering, Oklahoma State University, Stillwater, OK 74078, USA
[3] Homer L Dodge Department of Physics and Astronomy and Center for Semiconductor Physics in Nanostructures, University of Oklahoma, Norman, OK 73019, USA

E-mail: bret.flanders@okstate.edu

Received 20 January 2007, in final form 25 February 2007
Published 2 April 2007
Online at stacks.iop.org/Nano/18/175707

Abstract
We present a single-step, electrochemical approach to the growth and low contact resistance interconnecting of gold nanowires with targeted points on lithographic electrodes. Electron diffraction studies indicate that these nanowires are composed of face-centred cubic crystalline gold, and that the crystal structure is invariant along the wire lengths. Four-point resistance determinations of these electrode–nanowire–electrode assemblies consistently yield resistances of $<50\ \Omega$, and the contributions from the electrode–wire contacts are of the order of $10\ \Omega$. Atomic force microscopy was used to depict the structurally integrated nature of the electrode–wire contacts. This feature underlies the low electrode–wire contact resistances.

(Some figures in this article are in colour only in the electronic version)

1. Introduction

Nanowire synthesis is one of the most fundamental sub-processes of nanodevice fabrication. Of the many elements and compounds from which nanowires may be made, gold is technologically important for its low resistivity ($2.21\ \mu\Omega$ cm) [23], its inertness to attack by air and its resistance to sulfur-based tarnishing [12]. Additionally, gold is more biocompatible than most metals, rendering it suitable for implantation in [19, 27] or electrical interfacing with [13, 31, 42] cells and tissue in nano-biological applications [4, 33]. It may even prove feasible to perform novel electrophysiological characterizations of live cells by interfacing *multiple* gold nanowires with a *set* of targeted sites on a single cell, a challenging and long-standing goal [13, 30]. Finally, the well-established transport properties of *bulk* gold render the gold *nanowire* an ideal system in which to determine how metallic transport evolves with diminishing wire diameter [6]. These research areas would benefit from a *gold* nanowire fabrication methodology that permits the targeted placement of the wires in surrounding circuitry and that attains low contact resistance interconnecting of the wires with this circuitry. This combination of features will foster predictable nanowire behaviour in the assembled devices and it will enable reliable characterization of the nanowire-transport properties.

A variety of fabrication techniques have been developed in the past decade that yield high quality nanowires. Perhaps the most widely used nanowire synthesis is the vapour–liquid–solid method, where metallic nanodroplets catalyze the condensation, nucleation, and axial growth of vaporous growth material [44, 50]. This technique produces pristine arrays of single-crystal nanowires from a wide variety of materials [8, 15, 26, 41, 45, 46, 50, 51], arrangements that have been exploited in various photonic [16] and electronic [11] applications. Recently, this approach was refined to allow for the catalyst-free growth of metal-silicide nanowires [34]. In an alternative approach, porous substrates [48], nanotubes [49]. DNA and other biomolecules [39] have been used as templates in the formation of gold nanowires with very small diameters

[4] Author to whom any correspondence should be addressed.

and a range of intricate shapes. Thus, the value of vapour–liquid–solid and templated growth in nanowire fabrication is quite widely appreciated. However, a significant drawback to these established nanowire syntheses is that connecting the individual wires with external instrumentation and with other submicron components is most often accomplished by secondary processing steps that follow the wire synthesis. Two such approaches are known as blind sampling and piecewise-wire manipulation. These approaches limit the usefulness of the nanowires: blind sampling provides little control over the placement of the wires in the external circuitry, and piecewise manipulation is quite laborious. Furthermore, with both it is difficult to control the electrical properties of the electrode–nanowire junctions. Thus, methodology for the reproducible interconnecting of nanoscopic components with external circuitry is currently an area of intense research [11, 17, 36, 47].

Dielectrophoretic nanowire assembly was developed, in part, to address this problem. This technique exploits the voltage-induced chaining and fusing of nanoparticles into wires that span the gaps between opposing electrodes; thereby, the wire assembly and the electrode–wire contacts are accomplished in a single step [2, 14, 20]. This technique was later refined so that the wires could be grown between targeted points on the two electrodes [28, 29]. The transport properties of gold nanoparticle-based dielectrophoretic wires have been shown to have good reproducibility [28]. However, the resistivity of this material is ∼2000 $\mu\Omega$ cm [14, 28], three orders of magnitude greater than that of bulk gold. The resistive nature of these wires is due in large part to their particulate structure, as evidenced by the occurrence of the Coulomb blockade at reduced temperatures [28]. While such materials are needed for devices like variable capacitors [35], the directed growth of more highly conductive, metallic wires is of obvious importance in nanoelectronics.

We have recently demonstrated the directed growth of indium nanowires by an innovative technique that we call *directed electrochemical nanowire assembly* (DENA). This technique induces directional electrochemical deposition in simple salt solutions to produce the metallic wires [40] and, like the dielectrophoretic approach, enables the *single-step* growth and interconnecting of the wires with targeted points in external circuitry. Unfortunately, the measured resistances of these electrode–wire–electrode assemblies varied from a low of 500 Ω to a high of 28 kΩ. These 60 μm long wires had diameters that ranged from 370 to 560 nm and were shown to be single-crystalline indium; thus, the resistivity of these wires should be well described by (and almost certainly not less than) that of bulk indium (8.6 $\mu\Omega$ cm) [23]. Using this resistivity-value, the contribution of these 60 μm long wires to the resistances of the entire electrode–wire–electrode assemblies is calculated to vary between 20 and 50 Ω, depending on the wire diameter. This resistance range is much smaller than the measured kΩ-level resistances of these assemblies. A similar unacceptable range of resistances was found for electrode–wire–electrode assemblies made from Pd wires that were grown by a similar electrochemical technique in an independent study [3]. The resistances of these assemblies varied from a low of 1.7 kΩ to a high of 10.2 kΩ, even though the 20 μm long, 200 nm diameter Pd wires examined in this study have a calculated resistance of only 70 Ω, where the bulk Pd resistivity (10.5 $\mu\Omega$ cm) was used. Most probably, the electrode–wire–electrode resistances are much larger than the expected resistances of these metallic wires because the electrode–wire contacts in these assemblies are very resistive.

This lack of control over the contact resistance not only means that larger voltages are required to drive a given current through the wire, but could also qualitatively alter the electrical character of the wire. Nonmetallic transport behaviour (e.g. a negative temperature coefficient of resistivity) occurs in a variety of disordered conductors, such as granular metals [10], conducting polymer films [32] and nanoparticulate nanowires [28]. The disordered junctions between metal nanowires and electrodes can induce similar behaviour in metallic nanowires, as shown in a recent study of Pt nanowires interfaced with Au electrodes [5]. It is important that these interface-induced effects be minimized because they could mask temperature-dependent behaviour that arises due to other basic transport processes. Of particular significance to nanoscience is the conduction of electrons through very thin wires. As the wire diameter becomes comparable to the electronic mean free path, the resistivity is expected to increase [1, 6]. This occurs because, in addition to electron–phonon interactions (the canonical source of resistivity in metals), there is also the inelastic scattering of electrons at the surface of the conductor. As the electronic mean free path increases with decreasing temperature, the nanowire diameter becomes the limiting length scale for electronic motion, causing electron–surface scattering to dominate over electron–phonon interactions. This effect will manifest itself as a temperature-independent resistivity for a given wire, or as a resistivity that increases with decreasing wire diameter for a given material and temperature. Unambiguous experimental verification of this effect has yet to be reported and is, thus, a long-standing issue in nanoscience [5, 9, 25, 37]. Further characterization of this important process requires minimization of the electrode–wire contact resistances. Therefore, it is important that methodology for the low resistance interfacing of crystalline wires be established.

The present study reports on the single-step growth and interconnecting of near-single-crystalline *gold* nanowires with targeted sites in on-chip circuitry. The contact resistances of the electrode–nanowire–electrode assemblies investigated in this study are of the order of 10 Ω. This accomplishment circumvents the need for the post-synthesis processing that would otherwise be required to interface the wires with external circuitry. As a result, the precise characterization of the transport behaviour of such metallic nanowires is now possible.

2. Experimental details

2.1. Wire-growth circuitry

Figure 1 shows a diagram of the wire-growth apparatus. The optical micrograph depicts a gold nanowire bridging the 10 μm gap between the tips of the electrode pair. The electrodes are photolithographically deposited in 12-pair arrays on 0.5 mm thick quartz substrates and consist of a 100 nm thick base

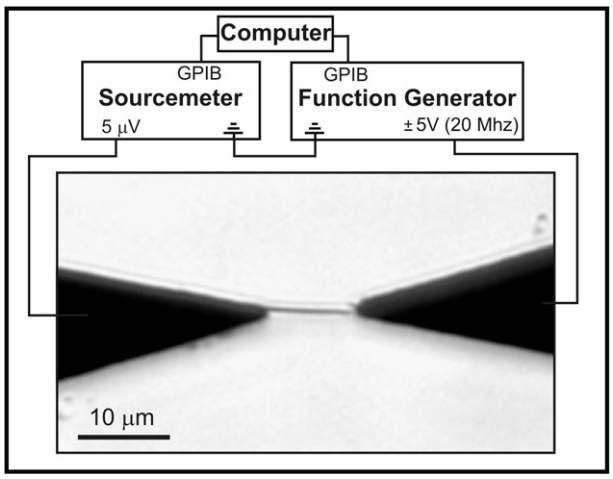

Figure 1. Diagram of the electrochemical wire-growth apparatus. The image is an optical micrograph of a gold wire grown between the tips of the lithographic electrodes. Each electrode tapers to a 1.5 μm wide tip and is connected via 120 μm wide conducting lines to macroscopic contact pads (not shown), enabling the interfacing of external instrumentation.

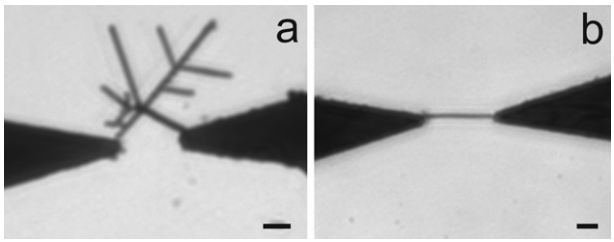

Figure 2. (a) An optical micrograph of a *dendritic structure* that was grown by the DENA technique when an 8 V signal was applied across a 0.050 M $HAuCl_4$ solution. The scale bar denotes 5 μm. (b) An optical micrograph of a *needle-shaped wire* that was grown under the same experimental conditions except that a reduced voltage amplitude of 6 V was used to initiate growth, and the voltage was reduced to 2 V as the wire grew across the gap. The scale bar denotes 5 μm.

layer of Ti and a 500 nm thick top layer of Au. The deposited metal was annealed by exposing the chip to a 425 °C argon atmosphere in a tube furnace for 10 min, rendering the electrodes resistant to electrochemical degradation during wire growth [28]. After depositing a 10 μl drop of 0.050 M aqueous $HAuCl_4 \cdot 3H_2O$ solution across the electrodes, an alternating voltage is applied across the gap in order to induce growth. The alternating lead of the function generator (Stanford Research Systems DS 345) is connected to the electrode from which growth is desired (the right electrode in figure 1). The other electrode (i.e. the left electrode in figure 1) is effectively grounded; that is, a very small (5 μV) voltage is applied to the left electrode (as explained below), but this signal does not affect wire growth. A 20 MHz square-wave voltage was used to induce the growth of all the wires investigated in this study, and a LabView program (described below) was employed to actively adjust the function generator during wire growth. This approach enabled reproducible contacts to be made between the wire and the electrodes. The wire spanning the gap shown in figure 1 was imaged on an inverted microscope (Leica, IRB) equipped with a digital camera (Hamamatsu, Orca ER II).

2.2. Electronics for attaining low contact resistances

In order to establish good contact between the wire and the electrodes, the alternating voltage signal is actively adjusted as the wire grows across the gap. The LabView program responsible for this task rapidly terminates the alternating voltage after the nanowire bridges the gap, thus preventing excessive current from being driven through the electrode–nanowire–electrode assembly. To grow a wire, the user manually increases the amplitude of the 20 MHz square-wave voltage signal to ∼5 V, or until wire growth is observed (which usually takes ∼30 s). As the wire grows across the gap, the user then reduces the voltage amplitude to ∼2 V in order to suppress the tendency for these wires to branch. The feedback signal for the control program is a small, cross-gap direct current. The voltage source meter (Keithley 2400) applies a small DC voltage (+5 μV) to the left electrode, as indicated in figure 1. This small voltage does not perturb the wire-growth process. With this DC voltage, the source meter can actively measure the DC current between electrodes. Before the wire bridges the gap, the cross-gap current is <10 nA; however, when the wire contacts the left electrode, the feedback current increases dramatically. On reaching a specified value for the feedback current (we have found that 1 μA is a good value for 10 and 15 μm long wires), the program terminates the alternating voltage. This procedure prevents excessive alternating current from being driven through the wire when it bridges the gap, as such currents would break the electrode–wire contacts which function as electrical fuses in this circuit. As will be shown below, this automated procedure allows for consistent minimization of the contact resistance between the wires and the electrodes. This program is conceptually similar to that used previously in the dielectrophoretic growth of nanowires [20].

3. Results and discussion

3.1. Structural analysis

The needle-shaped wire depicted in figure 1 grows by a dendritic solidification process. For a given electrode-gap and geometry, variation of the voltage amplitude, its frequency, and the $HAuCl_4$ concentration gives rise to a range of wire morphologies. For example, figure 2(a) depicts a highly branched, tree-shaped structure that is typical of metallic dendrites [7]. This structure grew across the 10 μm electrode gap upon application of an 8 V, 20 MHz voltage signal to a 0.050 M $HAuCl_4$ solution. This voltage signal was held constant as the wire grew across the gap. In contrast, figure 2(b) depicts a wire that was grown under the same experimental conditions except that a reduced voltage amplitude of 6 V was used to initiate growth and the voltage amplitude was reduced to ∼2 V as the wire grew across the gap. This branchless wire has a needle-shaped morphology. Hence, this result suggests that reducing the voltage amplitude during growth either suppresses side-branching or lengthens the side-branch spacing to a value greater than the electrode gap length. Articulation of the mechanism underlying these

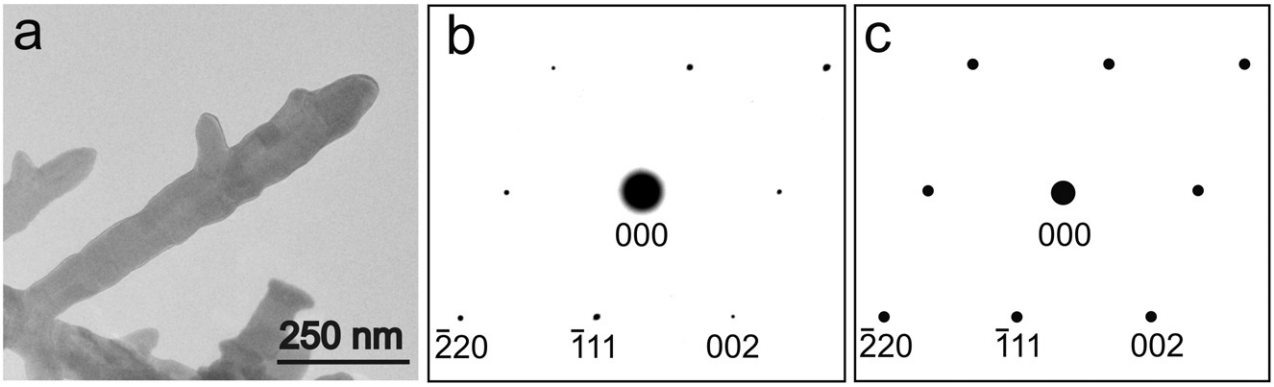

Figure 3. (a) A 764 nm long wire, transferred to a TEM grid. (b) The measured diffraction pattern of the wire segment in (a). For the sake of maintaining clarity during reproduction, the contrast of this pattern has been inverted. A 1.0 μm aperture was used to define the electron beam diameter for this measurement. (c) The calculated diffraction pattern of crystalline gold, observed from the [110] direction.

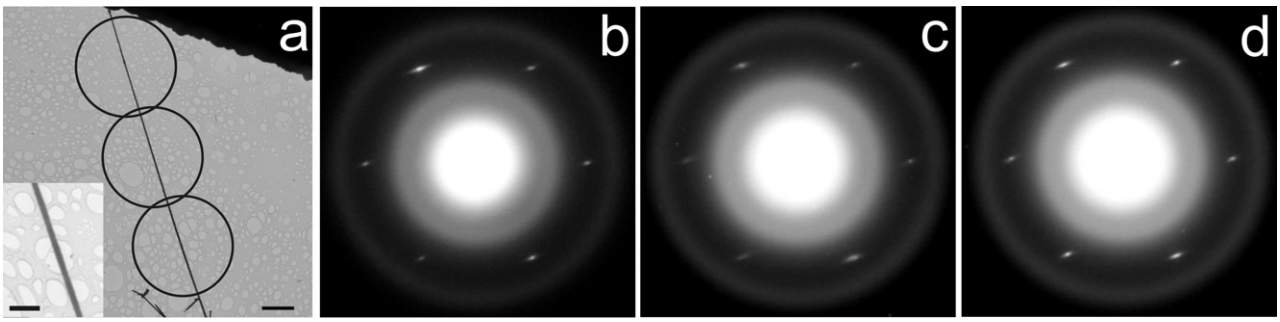

Figure 4. (a) A TEM micrograph of a 19.3 μm long gold wire on a TEM grid. The scale bar denotes 2 μm. The inset depicts an enlarged view of the central portion of this wire. The scale bar in the inset denotes 200 nm. The selected area diffraction patterns in (b)–(d) were measured from the regions in panel (a) denoted by the (b) lower circle, (c) middle circle and (d) upper circle. A 6.6 μm aperture was used to define the electron beam diameter for this study.

behaviours lies beyond the scope of this study; however, the needle-shaped structure is a well characterized member of the many possible morphologies that may be produced via dendritic solidification [21, 22]. Furthermore, we have also observed voltage-induced suppression of dendritic side-branching with In nanowires [40], suggesting that this effect is a general characteristic of the DENA technique.

A 200 kV transmission electron microscope (TEM) made by JEOL (JEM-2000FX) was used to obtain detailed crystallographic information of the needle-shaped wires. Because the quartz substrates of the electrode arrays are not thin enough to transmit the electron beam, it was necessary to transfer the wires to TEM grids. Transfer was accomplished by using a micromanipulator to slide a TEM grid (Ted Pella) across the wire-laden electrode gap. This process broke the wires off of the electrodes and deposited them onto the grid. Figure 3(a) shows a TEM micrograph of a single wire that was mounted in this manner. This image was collected with the electron beam normal to the sample plane. The wire is needle-shaped with sparse side-branching, having a diameter of 143 nm. Although much longer wires were present on the grid, this wire was chosen because it resided over a hole in the carbon netting of the grid. Hence, a clean diffraction pattern without contributions from the amorphous netting could be attained.

The composition of this wire was determined via electron diffraction. Figure 3(b) depicts a selected area electron diffraction pattern collected from the wire segment in figure 3(a). Figure 3(c) shows a simulated [110] diffraction pattern that was calculated using a commercial software package (Virtual Laboratories, Desktop Microscopist), requiring as input the camera length (790.8 mm), the electron wavelength (2.51×10^{-3} nm) and the known structural parameters of crystalline gold: a face centred cubic crystal structure, with $a = b = c = 0.407\,86$ nm, belonging to symmetry group $Fm\bar{3}m$ [38]. The experimental and simulated diffraction patterns are in excellent quantitative agreement with each other. For example, on the TEM film the distances of the $\bar{1}11$ and 002 spots from the 000 spot are 8.40 and 9.73 mm, respectively; the angle subtended by these diffracted spots is $54.2° \pm 0.4°$. The corresponding calculated values are 8.43 mm, 9.73 mm and 54.7°. The error for each of these quantities is less than 0.91%. This close quantitative agreement indicates that the wire is composed of crystalline gold. Of 10 wires examined in this manner, all were face-centred cubic crystalline gold.

To determine the structural continuity of the crystalline regions of these wires, selected area diffraction patterns were collected from successive positions along the wire lengths, using an area selection aperture with a 6.6 μm diameter. Figure 4(a) depicts a TEM micrograph of a 19.3 μm long gold nanowire grown by the DENA technique. The inset shows

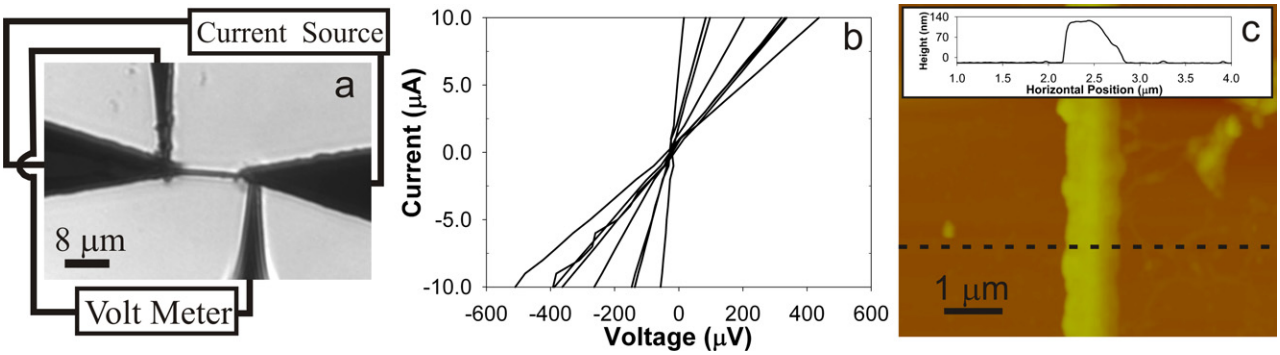

Figure 5. (a) Layout for a four-point resistance measurement of a nanowire. The optical micrograph depicts a gold wire bridging a 10 μm electrode gap. The microprobes make contact with the electrodes near the electrode–nanowire junctions. (b) Four-point current–voltage profiles (solid lines) of 8 different nanowires grown with the feedback-controlled growth procedure. (c) A topographical image of a gold nanowire. The inset depicts its height profile along the dashed line in the image. The average height of this wire along the length shown in this image is used for its diameter.

an enlarged view of the central portion of this wire. The diameter is 75.4 nm. Figures 4(b)–(d) represent diffraction patterns captured from the lower, middle and upper sections of the wire shown in figure 4(a), respectively. Analyses of the discrete patterns in figures 4(b)–(d) indicate that all three diffraction patterns result from crystalline gold observed from the ⟨111⟩ direction (confirming the compositional assignment made above). The diffuse rings in these images result from the amorphous carbon strands of the TEM grid beneath the wire segment, which are visible in panel (a). Moreover, in each of the three images, the six spots positioned at the hexagonal vertices, constituting the ⟨111⟩ diffraction pattern, are identically oriented. Furthermore, they are located the same distances from the 000 spot and no double (or multiple) sets of diffracted spots are visible. These observations indicate that the crystal structure of this wire segment does not deviate along its 19.3 μm length. Of 10 wire segments examined in this manner, all 13 μm or greater in length, the crystal structures were found to be similarly invariant along the length of each segment. These results are consistent with the conclusion that the wires grow as *single crystals* of pure gold, as was previously observed with electrochemically grown indium wires [40]. However, one of these samples (i.e. that shown in figure 3(a)) exhibited a diffraction pattern with two identical but slightly separated sets of spots when it was rotated and observed from the [0$\bar{1}$1] direction. This observation indicates that this wire has a twinned crystal structure. Determination of the extent to which twinning occurs in these wires awaits the orientationally resolved, transmission electron diffraction-based study of many wires and, therefore, lies beyond the scope of this study. Nevertheless, this study clearly demonstrates that the DENA technique produces lengthwise structurally invariant gold nanowires.

3.2. Charge-transport properties

The resistances of these electrode–nanowire–electrode assemblies are very low—consistently less than 50 Ω (as compared to the kΩ resistances of electrochemically grown In and Pd nanowires); hence, the four-point method has been used to characterize the transport properties. Figure 5(a) depicts the layout for these measurements. The current was supplied by connecting the leads of a current source (Keithley 2400) to the contact pads on the electrode arrays. The on-chip distance between a contact pad and an electrode tip was 14 mm. Two high precision manipulators were used to interface submicron-sized probes (MicroManipulator) to the electrode pairs, with each contact point being ∼100 μm from each tip. These probes served as the leads of a microvolt meter (Keithley 2400). With this set-up, the voltage difference between these contact points was measured as a function of the pad-to-pad current to generate the four-point current–voltage profiles.

The solid lines in figure 5(b) depict the four-point current–voltage profiles of eight electrode–nanowire–electrode assemblies that were grown via the feedback-controlled voltage application procedure. These measurements were conducted at 298 K on dried samples that were characterized by 10 μm electrode gaps. The steep slopes of these profiles indicate that all 8 electrode–wire–electrode resistances R_M are less than 50 Ω. These measured values for R_M are 3.6, 12.2, 13.0, 23.4, 35.0, 35.8, 36.0 and 47.8 Ω. Conversely, the resistance of a typical electrode–nanowire–electrode assembly that was grown without using feedback-controlled growth is ∼40 kΩ. A similar study of electrochemically grown Pd nanowires determined that a typical electrode–nanowire–electrode assembly had a resistance of 1.69 kΩ, whereas the resistance of the 20 μm long, 200 nm wide Pd wire would have been ∼70 Ω were the contact resistances negligible [3]. The low values for the electrode–nanowire–electrode resistances shown in figure 5(b) strongly suggest that the electrode–wire contacts are well made and, thereby, the kΩ-level resistances attained previously are avoided. As we will show below, the electrode–wire contact resistance is of the order of 10 Ω.

Further analysis of the current–voltage profiles enables the wire–electrode contact resistances to be extracted. As figure 5(a) suggests, these four-point resistance determinations reflect five contributions: the resistance of the nanowire R_W, the two electrode–wire contact resistances expressed here as $2R_C$, and the resistances of the electrode segments between the right and left microprobes and the nanowire; these are denoted by R_{ER} and R_{EL}, respectively. As these resistances are all in series, the measured resistance R_M may be expressed as $R_M = R_{ER} + R_{EL} + R_W + 2R_C$. (Because

Table 1. A summary of the various contributions to the measured resistances R_M of five different electrode–nanowire–electrode assemblies. The R_{ER} and R_{EL} values were each measured independently. The R_W values were determined by measuring the length and diameter of each of the wires and invoking the resistivity for bulk gold. The total contact resistance $2R_C$ was determined by subtracting R_{ER}, R_{EL} and R_W from R_M.

Wire	R_M (Ω)	R_{ER} (Ω)	R_{EL} (Ω)	R_W (Ω)	$2R_C$ (Ω)
1	13.0	9	7	2	−5
2	23.4	9	8	1	5
3	35.0	10	9	5	11
4	35.8	10	8	4	14
5	36.0	8	6	22	0

negligible current flows through the microprobes in this four-point technique, the microprobe–electrode contact resistances are not factors in these measurements [18].) As we will show, it is straightforward to solve this equation for $2R_C$, in order to estimate the contact resistance of the electrode–nanowire–electrode assemblies.

R_{ER} and R_{EL} are determined as follows. Using a probe station, we have determined the resistance per length of the 120 μm wide conducting lines to be $r_0 = 0.010\ \Omega\ \mu\text{m}^{-1} \pm 0.001\ \Omega\ \mu\text{m}^{-1}$. However, these lines taper to form the 1.5 μm wide tips, giving rise to a position-dependent resistance along the taper. As derived in the appendix, this geometry leads to the expression

$$R_E = r_0 L \ln\left(\frac{x_2}{x_1}\right) \quad (1)$$

for the resistance of the tapered electrodes. Here, the taper length $L = 250\ \mu$m. x_2 is the distance between the microprobe–electrode contact point and the position of a perfectly sharp electrode tip (the apex). Due to the finite lithographic resolution that results in the 1.5 μm wide tips, the actual electrode tip is 3.1 μm nearer the microprobe–electrode contact point than the apex. x_1 is the distance between the electrode–wire contact point and the apex (taken to be 3.1 μm when the wire precisely contacts the actual 1.5 μm wide tip, as explained in the appendix). For the right electrode in this particular measurement, the nanowire contacted the right electrode precisely at its tip, so $x_1 = 3.1\ \mu$m, and the microprobe contacted the electrode 65 μm from the (actual) tip, so $x_2 = 65\ \mu\text{m} + 3.1\ \mu\text{m} = 68.1\ \mu$m. Thus, $R_{ER} = 8\ \Omega$. For the left electrode, this nanowire grew 5 μm past the tip before making contact with the electrode, so $x_1 = 3.1\ \mu\text{m} + 5\ \mu\text{m} = 8.1\ \mu$m. The microprobe contacted the electrode 95 μm from the tip, so $x_2 = 95\ \mu\text{m} + 3.1\ \mu\text{m} = 98.1\ \mu$m. Thus, $R_{EL} = 6\ \Omega$. There is a precision $\pm 2\ \Omega$ associated with these R_{EL} and R_{ER} determinations due to the uncertainty in r_0.

R_W is determined as follows. We have shown that these wires grow as crystalline gold; additionally, the mean free path of room temperature gold is ∼30 nm [43], much smaller than the wire diameters (the smallest of which is 75 nm), so size-induced effects on the resistivity of the gold wires are not expected, and the resistivity ρ of the nanowire may reasonably be equated to that of bulk gold, 2.21 $\mu\Omega$ cm. By measuring the length l and cross-sectional area A of the nanowire, R_W is determined via the equation $R_W = \rho l/A$. Atomic force microscopy (AFM) was used to determine the nanowire diameters. A typical AFM-based topographical image is shown in figure 5(c). (It is the $R_M = 36.0\ \Omega$ wire that is depicted here.) The line-cut in the inset shows that the height of this wire relative to the glass substrate is 133 nm. Moreover, the average height of this wire along the 5 μm length shown in this image is 140 nm ± 20 nm. Due to the absence of tip-convolution effects in the vertical dimension, the vertical features of AFM-based images reflect the size of nanoscale samples much more accurately than features in the image plane. Therefore, we model the wire as a cylinder with a 140 nm diameter and a 15.6 μm length; the length was determined from an optical micrograph of the wire (not shown). Hence, R_W is found to be 22 Ω. There is a precision ±5 Ω associated with the R_W determinations due to the uncertainty in the wire diameter.

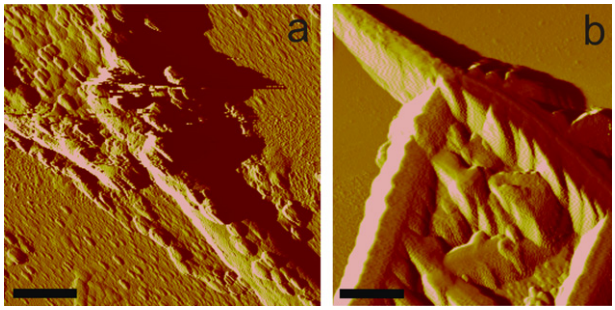

Figure 6. Atomic force micrographs collected in amplitude mode of (a) the junction between the alternating electrode and a DENA-fabricated gold nanowire and (b) the junction between the grounded electrode and a DENA-fabricated gold nanowire. The scale bars denote 1 μm.

Inserting these values for R_W, R_{ER} and R_{EL} into the equation for R_M yields a value for the total contact resistance for this 36.0 Ω assembly of $2R_C = 0\ \Omega$. As presented in table 1, four other wires, i.e. those with $R_M = 13.0$, 23.4, 35.0 and 35.8 Ω, were also analysed in this manner. This analysis indicates that the 13.0 Ω assembly had a total contact resistance of $2R_C = -5\ \Omega$, the 23.4 Ω assembly had a total contact resistance of $2R_C = 6\ \Omega$, the 35.0 Ω assembly had a total contact resistance of $2R_C = 11\ \Omega$, and the 35.8 Ω assembly had a total contact resistance of $2R_C = 14\ \Omega$. Due to the uncertainties in the wire diameters and r_0, these determinations of $2R_C$ have a precision of $\pm 6\ \Omega$; thus, the unphysical negative $2R_C$ value for the 13.0 Ω assembly reflects this uncertainty. This work demonstrates the ability of the DENA technique to establish electrode–nanowire contacts with consistently small contact resistances. Finally, it should be noted that these estimates for $2R_C$ reflect the total contact resistance of the electrode–nanowire–electrode assembly, which contains two electrode–nanowire contacts. Thus, the maximum contact resistance of any individual electrode–wire junction is between R_C and $2R_C$.

The feedback-controlled voltage-termination procedure achieves continuous physical contact between both electrodes and the nanowire and, thereby, achieves low resistance interconnecting in the electrode–wire–electrode assemblies. Figure 6(a) depicts an atomic force micrograph (collected in amplitude mode) of the junction between the *alternating* electrode and a DENA-fabricated nanowire. The electrode

occupies the upper left portion of this image, and the wire extends from the electrode tip to the lower right corner of the image. This micrograph shows that the junction between the electrode and the wire is structurally well-integrated. DENA wires grow from the alternating to the grounded electrodes, so it is not surprising that this junction is structurally continuous: structural continuity establishes electrical continuity—a necessity for wire growth in this electrochemical technique. The fact that wire growth occurs at all suggests that good structural integrity is attained at the alternating electrode–nanowire junction. We have examined 12 alternating electrode–nanowire junctions via atomic force microscopy; all exhibited good structural integrity between the apex of the alternating electrode and the nanowire. Figure 6(b) depicts an atomic force micrograph of the junction between the *grounded* electrode and a DENA-fabricated nanowire. This is the electrode to which the wire grows in the DENA technique. The electrode occupies the lower right portion of this image and the wire extends from the upper left corner to the apex of the grounded electrode, where it branches into two segments. Each segment grows beyond the apex while maintaining direct contact with the surface of the grounded electrode. This extensive, physical contact between the branches and the electrode surface underlies the low electrode–wire contact resistance that characterizes this technique. We have used atomic force microscopy to examine eight grounded electrode–nanowire junctions for electrode–nanowire–electrode assemblies that were fabricated using the feedback-controlled voltage-termination procedure. All were characterized by branching into multiple (2–4) segments at the grounded electrode apex and close physical contact between each segment and the surface of the grounded electrode. Conversely, electrode–wire–electrode assemblies that were produced without employing the feedback-controlled voltage termination procedure and that had large (∼40 kΩ) resistances failed to exhibit either of these structural properties at the grounded electrode–wire junction.

4. Conclusions

This work establishes an innovative, electrochemical approach to growing crystalline gold nanowires between targeted sites in on-chip circuitry. Moreover, this single-step, automated procedure for growing and interconnecting nanowires reduces the electrode–wire contact resistance to the order of 10 Ω, eliminating the need for secondary processing steps that serve to interface the wires with the electrodes. It is the structurally integrated nature of the electrode–nanowire contacts that gives rise to the low electrode–wire contact resistance. As the directed growth and interfacing of wires is not easily attainable with other crystal-growth techniques, such as the vapour–liquid–solid mechanism [24], this work is expected to prove useful in applications requiring the *in situ* growth of near-single-crystalline interconnects. In particular, this capability is expected to critically facilitate future studies of diameter-dependent charge transport in metallic nanowires.

To our best knowledge, the sub-15 Ω contact resistance of the electrode–nanowire–electrode assemblies described here is the smallest that has been attained by any *single-step* growth and interconnecting approach. We expect to reduce this resistance even more in a future effort that will focus on more extensive imaging of the electrode–wire contacts. By correlating the structure of these contacts with growth parameters such as the critical feedback current, the salt concentration and the frequency of the alternating voltage, we expect to delineate an experimental protocol for precisely controlling the structure of the electrode–wire junctions. This capability will allow for the consistent realization of electrode–wire interfaces with resistances of a few ohms or less.

Acknowledgments

This work was supported by the National Science Foundation (NER-304413 and PHY-646966) and Oklahoma EPSCoR (EPS-132354). We thank Yuguang Zhao for applying his expertise to the photolithographic fabrication of the electrode arrays, and we thank Mike Lucas for the care taken in machining the chip-transfer system required to anneal the chips in the tube furnace. We also gratefully acknowledge use of the Samuel Roberts Noble Electron Microscopy Laboratory of the University of Oklahoma.

Appendix. Resistance of tapered electrodes

A derivation of equation (1), the expression for the resistance of a tapered electrode, is provided in this appendix. We calculate the resistance of the tapered electrodes, R_{ER} and R_{EL} as follows. A scaled diagram of a tapered electrode is depicted in figure A.1(a). The untapered conducting lines have a width $2W$ of 120 μm, and the taper occurs over a distance L of 250 μm, such that the width linearly decreases from 120 μm to a tip width of 1.5 μm. The resistance per length r_0 of the untapered portion of the electrodes is 0.010 Ω μm^{-1}. However, because the cross-sectional area A of a line decreases as it tapers, its resistance increases, in accordance with the formula $R(x) = \rho l/A(x)$, where x is defined in figure A.1(a), and $A(x) = w(x)t$. $w(x)$ is the width of the electrode and t is its thickness, which we assume to be constant. The lines taper linearly, so $w(x)$ varies with a slope of $m = W/L$. Therefore, the width of the electrode at any given position x along the taper is

$$w(x) = 2mx. \tag{A.1}$$

$R(x)$ is inversely proportional to $w(x)$, so the resistance per length $r(x)$ at any point x along the taper is

$$r(x) = r_0 \frac{2W}{w(x)}, \tag{A.2}$$

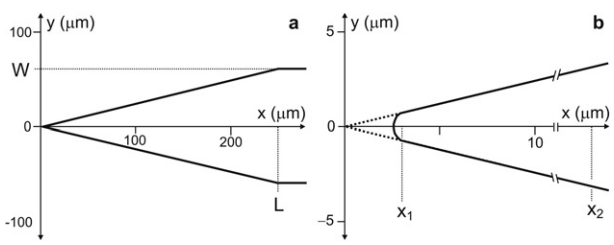

Figure A.1. (a) Diagram of the electrode geometry, showing the uniformly wide conducting line tapering to a sharp tip. (b) An expanded view of the tip region of the electrode. The dashed line denotes the profile of a perfectly sharp tip, while the solid line designates the blunter profile of an actual tip.

where $r_0 = 0.010\,\Omega\,\mu\text{m}^{-1}$. We obtain the resistance R_E of the electrode region that exists between the microprobe and wire contact points by integrating equation (A.2) over the electrode length of interest:

$$R_E = \int_{x_1}^{x_2} r(x)\,\mathrm{d}x, \tag{A.3}$$

where x_1 and x_2 are the positions at which the nanowire and the microprobe make contact with the electrodes, respectively. On substitution of equations (A.1) and (A.2) into (A.3), the electrode resistance is found to be

$$R_E = r_0 L \ln\left(\frac{x_2}{x_1}\right). \tag{A.4}$$

It should be noted that, because the tips taper to a finite width of 1.5 μm, x_1 is at least 3.1 μm, so equation (A.4) is never divergent; as figure A.1(b) shows, this minimum value is the horizontal distance from the electrode position where the width is 1.5 μm to the theoretical apex of a perfectly sharp tip. In practice, x_1 and x_2 are determined by optical microscopy.

References

[1] Andrew E R 1949 *Proc. Phys. Soc.* A **62** 77–88
[2] Bezryadin A, Westervelt R M and Tinkham M 1999 *Appl. Phys. Lett.* **74** 2699–701
[3] Cheng C, Gonela R K, Gu Q and Haynie D T 2005 *Nano Lett.* **5** 175–8
[4] Chithrani B D, Ghazani A A and Chan W C W 2006 *Nano Lett.* **6** 662–8
[5] DeMarzi G, Iacopino D, Quinn A J and Redmond G 2004 *Appl. Phys. Lett.* **96** 3458–62
[6] Dingle R B 1950 *Proc. R. Soc.* A **201** 545–60
[7] Doherty R D 1975 *Crystal Growth* 2nd edn ed B R Pamplin (New York: Pergamon)
[8] Duan X and Lieber C M 2000 *Adv. Mater.* **12** 298–302
[9] Durkan C and Welland M E 2000 *Phys. Rev.* B **61** 14215
[10] Dynes R C and Garno J P 1981 *Phys. Rev. Lett.* **46** 137–40
[11] Goldberger J, Hochbaum A I, Fan R and Yang P 2006 *Nano Lett.* **6** 973–77
[12] Greenwood N N and Earnshaw A 1984 *Chemistry of the Elements* (New York: Pergamon)
[13] Gross G W, Wen W Y and Lin J W 1985 *J. Neurosci. Methods* **15** 243–52
[14] Hermanson K D, Lumsdon S O, Williams J P, Kaler E W and Velev O D 2001 *Science* **294** 1082–6
[15] Hong L, Liu Z, Shang X T and Hark S K 2006 *Appl. Phys. Lett.* **89** 193105
[16] Huang M H, Mao S, Feick H, Yan H, Wu Y, Kind H, Weber E, Russo R and Yang P 2001 *Science* **292** 1897–9
[17] Jin S, Whang D, McAlpine M C, Friedman R S, Wu Y and Lieber C M 2004 *Nano Lett.* **4** 915–9
[18] Keithley J E 2002 *Low Level Measurements Handbook* (Cleveland, OH: Keithley Instruments)
[19] Kouklin N A, Kim W E, Lazareck A D and Xu J M 2005 *Appl. Phys. Lett.* **87** 173901
[20] Kretschmer R and Fritzsche W 2004 *Langmuir* **20** 11797–801
[21] Libbrecht K G and Tanusheva V M 1998 *Phys. Rev. Lett.* **81** 176–9
[22] Libbrecht K G and Tanusheva V M 1999 *Phys. Rev.* E **59** 3253–61
[23] Lide D R 1994 *The Handbook of Chemistry and Physics* 74th edn (Boca Raton, FL: Chemical Rubber Company)
[24] Miao W G, Wu Y and Zhou H P 1997 *J. Mater. Sci.* **32** 1969–75
[25] Molares M E T, Höhberger E M, Schaeflein C, Blick R H, Neumann R and Trautmann C 2003 *Appl. Phys. Lett.* **82** 2139–41
[26] Morales A M and Lieber C M 1998 *Science* **279** 208–11
[27] Obataya I, Nakamura C, Han S W, Nakamura N and Miyake J 2005 *Nano Lett.* **5** 27–30
[28] Ozturk B, Blackledge C, Grischkowsky D R and Flanders B N 2006 *Appl. Phys. Lett.* **88** 073108
[29] Ozturk B, Talukdar I and Flanders B N 2005 *Appl. Phys. Lett.* **86** 183105
[30] Patolsky F, Timko B P, Yu G, Fang Y, Greytak A B, Zhang G and Lieber C M 2006 *Science* **313** 1100–4
[31] Pine J 1980 *J. Neurosci. Methods* **2** 19–31
[32] Reghu M, Cao Y, Moses D and Heeger A J 1993 *Phys. Rev.* B **47** 1758–64
[33] Rosi N L, Giljohann D A, Thaxton C S, Lytton-Jean A K R, Han M S and Mirkin C A 2006 *Science* **312** 1027–30
[34] Schmitt A L, Bierman M J, Schmeisser D, Himpsel F J and Jin S 2006 *Nano Lett.* **6** 1617–21
[35] Seneor P, Lidgi N, Carrey J, Jaffres H, NguyenVanDau F, Friederich A and Fert A 2004 *Europhys. Lett.* **65** 699–704
[36] Shi J, Lu Y F, Yi K J, Lin Y S, Liou S H, Hou J B and Wang X W 2006 *Appl. Phys. Lett.* **89** 083105
[37] Smith P A, Nordquist C D, Jackson T N, Mayer T S, Martin B R, Mbindyo J and Mallouk T E 2000 *Appl. Phys. Lett.* **77** 1399–401
[38] Swanson H E, Fuyat R K and Ugrinic G M 1954 *National Bureau of Standards Circular* 539 vol 3 (Washington, DC: US Govt Printing Office) p 3
[39] Takahashi R and Ishiwatari T 2004 *Chem. Commun.* **12** 1406–7
[40] Talukdar I, Ozturk B, Mishima T D and Flanders B N 2006 *Appl. Phys. Lett.* **88** 221907
[41] Tang C C, Fan S S, Dang H Y, Li P and Liu Y M 2000 *Appl. Phys. Lett.* **77** 1961–3
[42] Thomas C A, Springer P A, Loeb G E, Berwald-Netter Y and Okun L M 1972 *Exp. Cell Res.* **74** 61–6
[43] Vancea J, Hoffmann H and Kastner K 1984 *Thin Solid Films* **121** 201–16
[44] Wagner R S and Ellis W C 1964 *Appl. Phys. Lett.* **4** 89–90
[45] Wang Y, Zhang L, Liang C, Wang G and Peng X 2002 *Chem. Phys. Lett.* **357** 314–18
[46] Wang Z L, Dai Z R, Gao R P, Bai Z G and Gole J L 2000 *Appl. Phys. Lett.* **77** 3349–51
[47] Whang D, Jin S, Wu Y and Lieber C M 2003 *Nano Lett.* **3** 1255–9
[48] Wirtz M and Martin C R 2003 *Adv. Mater.* **15** 455–8
[49] Wong T C, Li C P, Zhang R Q and Lee S T 2004 *Appl. Phys. Lett.* **84** 407–9
[50] Wu Y and Yang P 2001 *J. Am. Chem. Soc.* **123** 3156–66
[51] Xia Y, Yang P, Sun Y, Wu Y, Mayers B, Gates B, Yin Y, Kim F and Yan H 2003 *Adv. Mater.* **15** 353–89